**Showcasing research from Prof. Jian-Feng Chen's group at the Research Center of the Ministry of Education for High Gravity (HIGEE) Engineering and Technology, Beijing University of Chemical Technology, China.**

Metal-free catalytic oxidation of benzylic alcohols for benzaldehyde

A high-gravity rotating packed bed reactor was used for process intensification during the metal-free catalytic reaction, which provided more turbulent kinetic energy and faster surface renewal rate to improve the catalytic efficiency. This study reveals the possibility of combining metal-free catalysts and high-gravity technology for the green synthesis of chemicals.

ROYAL SOCIETY OF CHEMISTRY | Celebrating IYPT 2019

rsc.li/reaction-engineering
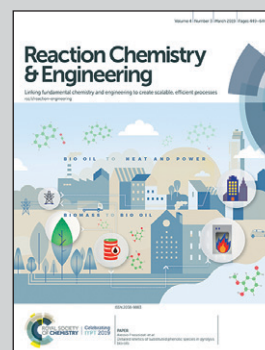
Metal-free catalytic oxidation of benzylic alcohols for benzaldehyde†

Zhiyong Wang,[ab] Jie Shi,[ab] Dan Wang, [iD] *[ab] Yuan Pu,[ab]
Jie-Xin Wang[ab] and Jian-Feng Chen*[ab]

Sulfurized graphene (SG) was employed as a metal-free catalyst for the liquid-phase catalytic oxidation of benzyl alcohol (BzOH) in the existence of hydrogen peroxide for the first time. The conversion efficiencies of BzOH at different reaction conditions were studied. SG was demonstrated to be among the best metal-free catalysts for this reaction in conversional stirred tank reactors with BzOH conversion of 18.2% (2 mg catalyst, 3 h, $T = 80\ ^{\circ}C$). A high-gravity rotating packed bed reactor was used for process intensification during the metal-free catalytic oxidation, and BzOH conversion increased from 5.56% to 20.86%. Both experimental and computational fluid dynamics simulations indicate that a high-gravity level can provide more turbulent kinetic energy and faster surface renewal rate to improve the catalytic efficiency. This study opened up the possibility of combining metal-free catalysts and high-gravity technology for the green synthesis of chemicals.

Introduction

The oxidation of alcohols to their corresponding high-value-added carbonyl compounds is an important reaction in the synthesis of fine chemicals and organic intermediates.[1–3] Benzaldehyde (BzH), for example, is in high demand in the dyestuff and pharmaceutical industries.[4–6] At present, the traditional synthesis processes of BzH mainly adopt the hydrolysis of benzal chloride derived from toluene chlorination, which introduce chlorinated impurities and cause environment pollution.[7–9] For the past few years, because of the increasing demand of high-quality BzH in the global market, the liquid-phase oxidation of benzyl alcohol (BzOH) by hydrogen peroxide (H_2O_2) has been considered as an important way to obtain BzH with high yield.[10–12] Till date, a variety of homogeneous and heterogeneous metal-based catalysts have been developed, such as Pd, Pt, and Co.[13–15] However, from a sustainability perspective, these catalysts are difficult to be widely applied in the industry because of their poor reserves and toxicity.[16–19] The sustainable development of the chemical industry necessitates green catalytic engineering, which refers to green catalysts and green processes for the industrial

manufacture of useful products and energy.[20,21] On one hand, as an alternative to traditional metal-based catalysts, carbon-based metal-free catalysts have drawn increasing attention in both scientific research and industrial chemical production processes.[22–24] Along with others, we have demonstrated that heteroatom-doped graphene is an efficient metal-free catalyst for energy conversion and chemicals manufacture.[25,26] Sulfurized graphene (SG), in particular, has exhibited remarkable catalytic performance in oxygen reduction reaction, catalytic reduction, esterification reaction, and photocatalysis due to the considerable polarization of the highest occupied molecular orbital and lowest unoccupied molecular orbital when the sulfur atom was doped on the graphene plane.[27] It would be worthwhile to investigate the catalytic kinetics and mechanism of SG for the liquid-phase oxidation of BzOH to develop new metal-free catalysts for the industry.

On the other hand, process intensification (PI) involving novel equipment and methods for achieving dramatic improvements in manufacturing processes has drawn widespread attention in recent years.[28,29] The study of novel equipment for enhancing heat and mass transfer for PI has been identified by the U.S. Department of Energy (DOE) as one of the 14 technological areas with transformative potential for closing the gap between current energy use and minimum energy requirements in chemicals manufacturing.[30–32] Therefore, it is also important to determine which type of reactor or technology is favored for the metal-free catalytic synthesis of chemicals. High-gravity technology based on the use of rotating packed bed (RPB) reactors has been demonstrated to be an efficient PI technology for reaction and separation.[33–36]

[a] *State Key Laboratory of Organic-Inorganic Composites, Beijing University of Chemical Technology, Beijing 100029, China. E-mail: wangdan@mail.buct.edu.cn, chenjf@mail.buct.edu.cn; Tel: +86 10 64449453, +86 10 64446466*
[b] *Research Center of the Ministry of Education for High Gravity Engineering and Technology, Beijing University of Chemical Technology, Beijing 100029, China*
† Electronic supplementary information (ESI) available. See DOI: 10.1039/c8re00265g

This journal is © The Royal Society of Chemistry 2019

React. Chem. Eng., 2019, 4, 507–515 | 507

However, studies involving SG for the catalytic oxidation of benzylic alcohols in RPB reactors have not been reported.

In this work, we reported the metal-free catalytic oxidation of BzOH for the synthesis of BzH by using SG as the catalyst. These SG catalysts were prepared by a well-developed ball-milling method, which can be easily scaled-up. H_2O_2 solution was used as the oxidizing agent and the BzOH conversions at different reaction conditions, such as temperature, catalyst dosage, reaction time, and stirring speed, were systematically studied. A density functional theory (DFT) calculation was used to determine that the doping of the sulfur atom into the carbon skeleton facilitates high catalytic activity. Moreover, a high-gravity RPB reactor was used to evaluate its potential applications in the catalytic oxidation of benzylic alcohols using metal-free SG as catalysts. The improved catalytic performance of SG in the RPB reactor was investigated by both experimental and computational fluid dynamics (CFD) simulations. This study reveals the possibility of combining metal-free catalysts and high-gravity technology for the green synthesis of chemicals.

Experimental section

Materials

Pristine graphite powder and sulfur (S_8) were purchased from Alfa Aesar. Concentrated sulfuric acid, hydrogen nitrate, carbon disulfide, H_2O_2, and BzOH were purchased from Sigma-Aldrich Co. All the reagents were analytically pure and used without further purification, unless otherwise mentioned. Deionized water prepared by a Hitech Laboratory Water Purification System DW100 (Shanghai Hitech Instruments Co., Ltd.) was used for all the experiments.

Preparation of SG

SG nanosheets were fabricated from the mixture of sulfur powder and commercial graphite with a modified ball-milling method.[26,37] Briefly, pristine graphite powders were simply modified by the same volume of nitric acid and sulfuric acid for several hours. The obtained products were added into the stainless steel of the planetary mill machine that contained a number of stainless steel balls with a diameter of 5 mm in the presence of sulfur powder. The stainless steel was charged with argon, and the ball-milling treatment was then performed by setting the speed at 500 rpm for two days. Thereafter, the obtained powder was further heated at 700 °C at the rate of 2 °C min^{-1} in a tube furnace for 3 h under an argon flow. Then, the sample was purified by HCl solution, and the resultant mixture was extracted by excess carbon disulfide to remove the excess sulfur powder. Finally, the product was freeze-dried at −50 °C for 5 h and then the pressure was decreased to 1.1 Pa after the prefreeze stage and heated up to 25 °C in a series at the rate of 1 °C h^{-1} for 20 h, 1.25 °C h^{-1} for 16 h, 1 °C h^{-1} for 10 h, and 5 °C h^{-1} for 5 h.

Characterization

Transmission electron microscope (TEM) images were obtained from a Hitachi H-9500 high-resolution TEM at an accelerating voltage of 300 kV. The surface morphology and elements distribution were examined by the combination of scanning electron microscope (SEM) and energy-dispersive X-ray (EDX) mapping on a Hitachi S-4700 SEM. A Thermo Fisher Nicolet 6700 FTIR system was used to record the Fourier-transform infrared (FTIR) spectra at room temperature. The Raman spectra were obtained from a Renishaw inVia Raman spectrometer with an excitation wavelength of 514 nm. X-ray diffraction (XRD) measurements were performed on a Shimadzu XRD-6000 X-ray diffractometer using Cu Kα radiation, and a VG Microtech ESCA 2000 was used to obtain the X-ray photoelectron spectroscopy (XPS) data.

Catalytic liquid-phase oxidation of BzOH

In a typical procedure, oxidation reactions were carried out at ordinary pressure in a 250 mL three-necked flask containing 1 mmol of BzOH, 2 mg of catalysts, 2 mL H_2O_2 (35 wt% in water), and 120 mL of water. Unless otherwise mentioned, the reactions were carried out in a water bath at 343 K with a reflux condenser for 3 h. Subsequently, the liquid mixture samples were filtered with a membrane filter and analyzed by high-performance liquid chromatography (HPLC, Waters 2690) equipped with a C18 chromatographic column. The conversion of BzOH and the selectivity and yield of BzH were calculated as per the following equations, respectively.

$$X_{BzOH} \text{ mol\%} = (C_{in} - C_{out})/C_{in} \times 100\% \qquad (1)$$

$$S_{BzH} \text{ mol\%} = Pi/{\textstyle\sum} Pi \times 100\% \qquad (2)$$

$$Y_{BzH} \text{ mol\%} = X_{BzOH} \text{ mol\%} \times S_{BzH} \text{ mol\%} \times 100\% \qquad (3)$$

Computational methods

All the calculations in this work are done in the DMol3 code based on the spin-unrestricted DFT method. We used the generalized gradient approximation (GGA) with the B3LYP hybrid functional in combination with the double numerical basis sets with polarization functions (DNP). In the process of calculations, the TS method for DFT-D correction was used. We set the convergence thresholds for the energy, force, and displacement to be 2.0×10^{-5} Ha, 0.004 Ha Å^{-1}, and 0.005 Å, respectively. Moreover, to improve the reliability of the simulation results, we used water (dielectric constant: 78.54) as the solvent to add a solvation model. The smearing of the electronic occupations was set to 0.005 Ha. For the other parameters, the default settings were used.

For modeling a system with one central carbon atom substituted by one sulfur atom, we employed a triangular graphene sheet comprising 82 atoms (including 60 C atoms, 21 H atoms for saturating edge C atoms, and 1 S atom). The search protocol was set to be linear synchronous transit (complete LST/QST) method. In order to obtain the minimum energy

508 | React. Chem. Eng., 2019, 4, 507–515

This journal is © The Royal Society of Chemistry 2019

pathway (MEP), we calculated the vibrational frequencies of each structure along the MEP at the same level to confirm that a transition state only has a single imaginary frequency.

Results and discussion

Fig. 1a shows the typical schematic representation of SG fabrication by the ball-milling operation. After the oxidation by nitric acid and sulfuric acid, pristine graphite exhibits certain expansion due to the increasing distance between the adjacent graphite layers and, therefore, the entire physical structure stability declines. When it is mixed with sulfur powder and milled by stainless steel balls, the original large layers are easily torn into fine sheets by the force of friction caused by the violent collisions between the graphite layers and stainless steel balls. From the digital photographs of the SG dispersion and graphite dispersion (Fig. 1b and S1†), we can observe that SG can maintain good dispersion for 2 h; nevertheless, pristine graphite dispersion became translucent and parts of it settled at the bottom, indicating that the stability of SG is higher than that of pristine graphite. It is because a large number of edge carbon atoms induced by the ball-milling operation can be exposed to
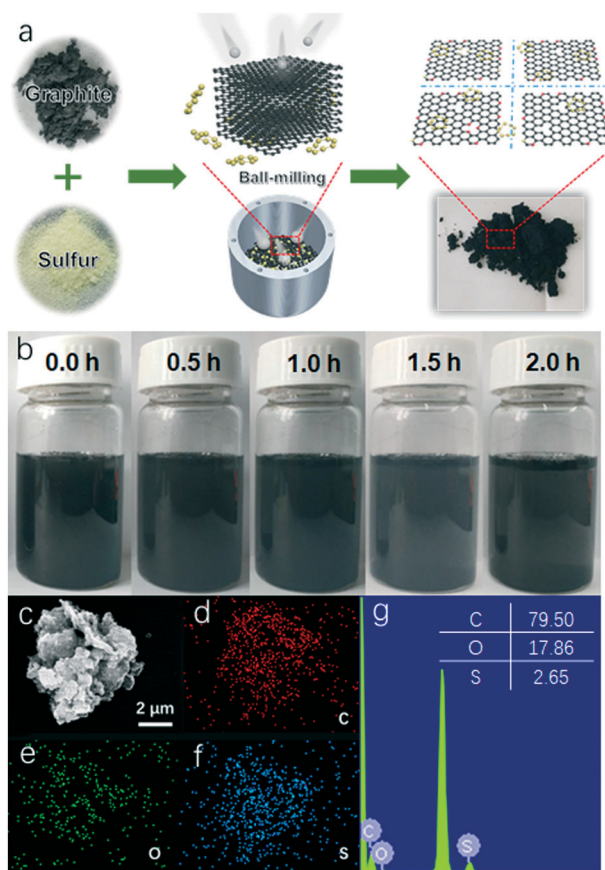

Fig. 1 (a) Schematic representation of SG fabrication by ball-milling method; (b) digital photographs of the SG dispersion for different durations (dispersions are 1 mg mL^{-1} in DI water, ultrasonic treatment for 30 min); (c) SEM image corresponding to the elemental mapping images of SG for (d) O, (e) C, and (f) S elements; (g) EDX spectroscopy of SG.

air and get oxidized to forming oxygen-containing functional groups, which induces SG with excellent hydrophilicity and dispersibility in water.[38] A successful synthesis of the SG nanosheets was investigated using a TEM instrument, as shown in Fig. S2.† The obtained SG possesses flake-like morphology with diameters ranging in hundreds of nanometers. The lattice fringe spacing of SG is determined to be 0.32 nm from HRTEM, which corresponds to the diffraction planes of sp2 graphitic carbon.[39] The SEM images (Fig. S3†) show that the pristine graphite powder exhibits a closely knit and agglomeration state, while on the same measuring scale, SG is much smaller in size. Generally, ball-milling can tear the original large graphite layers into fine sheets by the force of friction caused by the violent collision between the graphite layers and stainless steel balls; however, in the meantime, the temperature of some locations such as the layer edge may reach up to 1000 K.[40] At this moment, some fine graphite sheets can easily aggregate and get grinded into embedded spheroidal particles with diameters of 1–2 μm. Further, we carried out the SEM corresponding to energy dispersive spectroscopic (EDS) mapping. As shown in Fig. 1c–g, the oxygen, carbon, and sulfur elements are uniformly distributed on the surface of the sample with mass ratios of 17.86%, 79.50%, and 2.65%, respectively.

FTIR was used to obtain insights into the surface functional groups of the samples. Fig. 2a shows the FTIR spectra of pristine graphite and SG; the peaks observed at approximately 1384.8 cm^{-1}, 1728.1 cm^{-1}, and 1581.5 cm^{-1} in both graphite and SG samples can be attributed to the stretching vibrations of the C–O, C=O, and C=C bonds, respectively. However, the bands located at 887.2 cm^{-1}, 1120.5 cm^{-1}, and 578.6 cm^{-1}, corresponding to the stretching vibrations of the S–O, S=O, and C–S bonds, respectively, existed only in the SG sample, indicating that elemental sulfur is successfully doped into the graphene sheets.[41] The XRD patterns (Fig. 2b) reveal that pristine graphite possesses three peaks centered at 2θ values of 26.5, 44.6, and 54.7°, which can be assigned to the (002), (101), and (004) crystallographic facets of graphite.[42] The reduction in intensity for the graphitic characteristic peaks in the SG sample can be attributed to the exfoliation process during the ball-milling operation. However, with the simultaneous physical and chemical mixing between sulfur powder and graphite, there still exist some characteristic peaks at 2θ values of 10, 18, 22 and 28° when compared with the XRD pattern of pure sulfur powder (Fig. S4†).[42] Fig. 2c shows the Raman spectra of SG and graphite. Two bands at 1350.9 and 1580.1 cm^{-1} correspond to the D and G bands, which represent the defect degree and ideal degree of graphite structure, respectively. Therefore, the value of I_D/I_G can reveal that the SG sample exhibits more abundant defect sites than that in pristine graphite. In particular, the spectrum of SG was fitted to five components; except for the D and G bands, the other three bands located at 1236.7, 1513.4, and 1620.7 cm^{-1} represent ionic impurity, amorphous carbon, and disordered graphitic lattice, respectively.[43] Furthermore, the XPS spectrum has been utilized to investigate the heteroatom doping levels and bonding types of SG, as shown in Fig. 2d. The three pronounced peaks at 285, 532, and 168 eV

This journal is © The Royal Society of Chemistry 2019
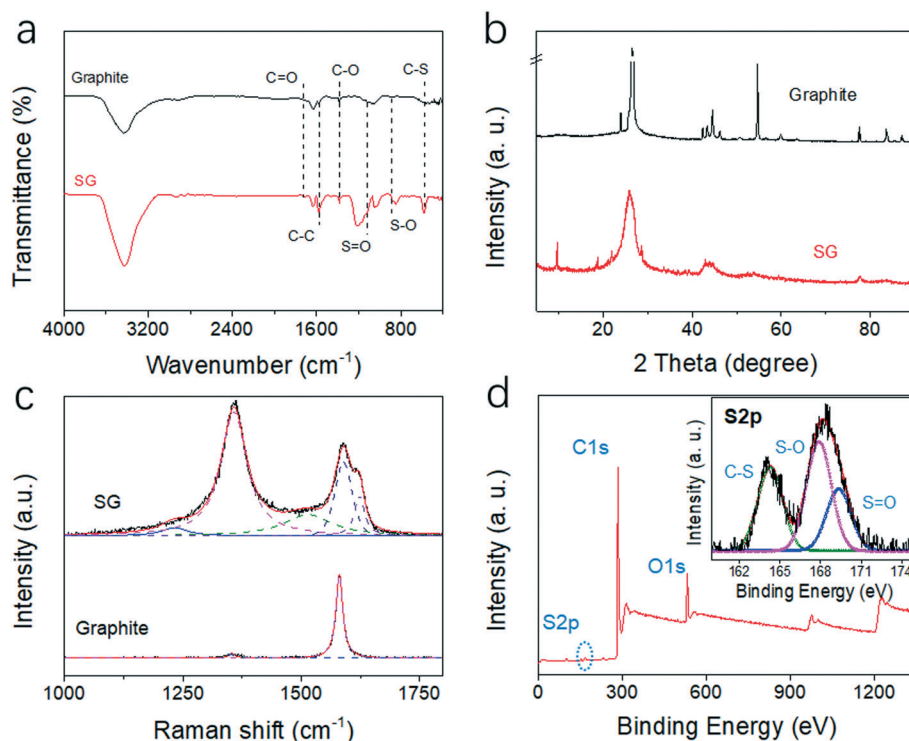
React. Chem. Eng., 2019, **4**, 507–515 | 509

Fig. 2 (a) Typical FTIR spectrum, (b) XRD patterns, and (c) Raman spectroscopy of SG and graphite; (d) XPS spectrum (inset: high-resolution S 2p peak) of SG.
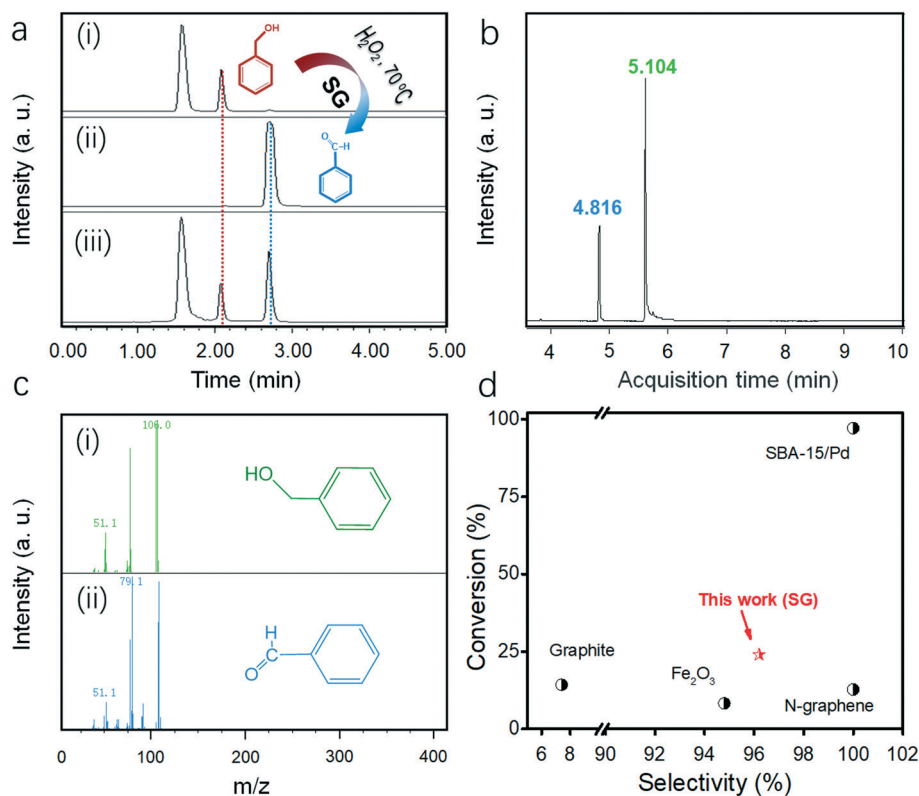

Fig. 3 (a) HPLC spectrogram of the (i) original BzOH, (ii) original BzH, and (iii) final product mixture; (b) GC-MS analysis of the final product mixture, and (c) corresponding mass spectrum of (i) BzOH and (ii) BzH; (d) catalytic oxidation performance of BzOH to BzH with different catalysts (SBA-15/Pd: 1 mg catalyst, 4 h, T = 80 °C; Fe$_2$O$_3$: 200 mg catalyst, 1.5 h, T = 100 °C; N-graphene: 30 mg catalyst, 10 h, T = 70 °C; graphite: 2 mg catalyst, 3 h, T = 70 °C; this work (SG): 2 mg catalyst, 3 h, T = 80 °C).

510 | *React. Chem. Eng.*, 2019, **4**, 507–515

This journal is © The Royal Society of Chemistry 2019

correspond to C 1s, O 1s, and S 2p, respectively. The inset shows a high-resolution image of the S 2p peak, which was fitted to three component peaks, namely, the C–S bond at 164.3 eV, S–O band at 167.9 eV, and S=O bond at 169.4 eV. In order to further confirm the functional groups in SG, the high-resolution C 1s and O 1s peaks are shown in Fig. S5.† As expected, the deconvolution of the C 1s peak demonstrates that the total C is in the form of graphitic C (284.8 eV) and oxycarbide (286.4 eV and 287.8 eV), which can also be observed in the high-resolution O 1s peaks at 531.9 eV and 533.5 eV.[44]

The aerobic liquid-phase oxidation of BzOH was catalyzed by the prepared SG sheets at 70 °C for 3 h with H_2O_2 as the sole oxidant and DI water as the solvent. Fig. 3a shows the HPLC spectral lines for the mixture solution before the reaction, well-known authentic BzH standards, and the mixture after reacting for 3 h. The substance at the residence time of about 1.6 min and 2.1 min correspond to H_2O_2 and BzOH, respectively. The results confirmed the presence of the target product at a residence time of about 2.7 min in the final solution. Furthermore, in order to determine the composition and proportion of the reaction mixture, the sample was also analyzed by gas chromatography-mass spectrometry (GC-MS) (Fig. 3b and c). The relative residence times listed in Table S1† indicate that the main byproduct is benzenedicarboxylic acid (BzA). Under this reaction condition, BzOH conversion (18.2%) and BzH selectivity (96.8%) were obtained by calculating the integral area ratios before and after the reaction, respectively. However, regardless of the conversion efficiency or selectivity, the catalytic performance of SG still lags far behind when compared with the noble-metal-based reference catalyst, namely, Pd-based catalysts, whose conversion efficiency is 97.1% (Fig. 3d).[45] When compared with nonprecious metals (conversion: 8.3%) and other metal-free catalysts (conversion: 12.8%), SG shows comparable selectivity and slight superiority in conversion efficiency.[46] However, Fe powder supported on nitrogen-doped carbon (Fe–N–C) reported by J. Xie *et al.* achieved excellent catalytic performance with 78% conversion of BzOH and about 90% selectivity toward BzH in the presence of 1 MPa O_2. In addition, the aerobic oxidation of BzOH was also conducted by using pristine graphite powder as the catalyst. Although the conversion of BzOH can reach 14.3%, the BzH yield is poor (1.1%). The decrease in BzOH is mainly due to the strong adsorption of graphite, which possesses weak activation capacity for H_2O_2. Therefore, there are almost no oxygen species (such as hydroxyl radicals) in the reaction solution, and the adsorbed BzOH cannot achieve the next transfer step, which results in the fairly low yield relative to the SG sheets. Moreover, when the oxidation is conducted at 70 °C for 3 h in the absence of any catalyst, the decrease in BzOH concentration was about 1.57%, and almost no BzH can be observed in the final reaction mixture.

For obtaining better performing SG catalysts, further optimization of the reaction conditions, such as reaction time, reaction temperature, catalyst dosage, and stirring speed, need to be carried out. Fig. 4a shows the values of BzOH conversion and BzH selectivity at different reaction times (from 1 h

to 5 h). Apparently, the selectivity is almost unchanged and is maintained over 95% with time. However, with regard to conversion, there is an induction period at the initial stage accompanied by the reaction. During this period, the reaction in the mixture solution involves two steps: the SG first absorbs H_2O_2 and activates it to form reactive oxygen species, which then reacts with the absorbed BzOH. However, with passing time, the SG catalyst gets deactivated and its BzOH absorption ability gets decreased, which results in a maintained concentration of BzOH in the reaction solution. Therefore, the conversion is increased at the initial stages and then remains unchanged for up to 5 h. To investigate the effect of reaction temperature on the catalytic activity and selectivity of SG, the reactions were conducted from 40 to 80 °C in increments of 10 °C. As shown in Fig. 4b, the conversion is dramatically affected by temperature. In general, BzOH conversion largely increased, but BzH selectivity
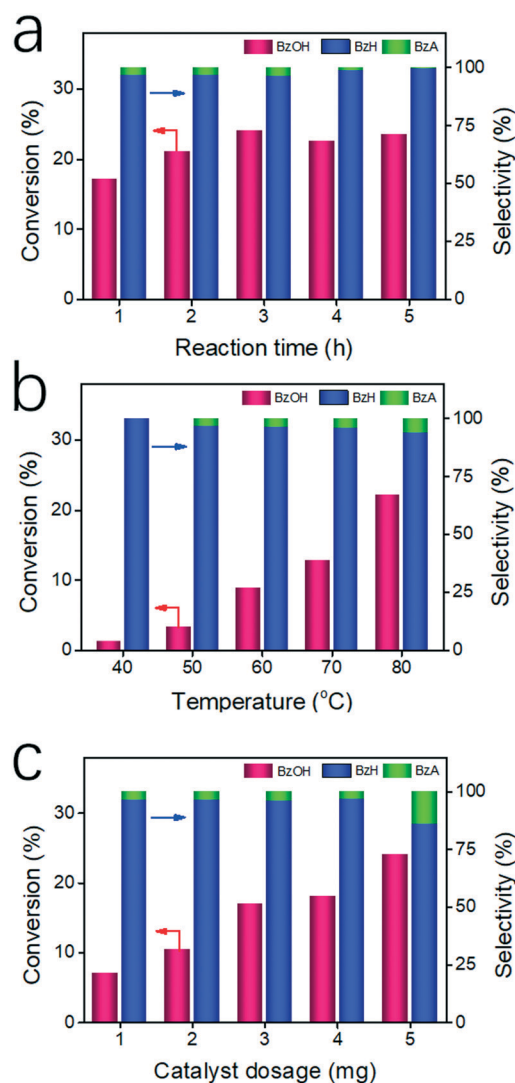

Fig. 4 Effect of (a) reaction time (reaction condition: 2 mg catalyst, T = 80 °C), (b) reaction temperature (reaction condition: 2 mg catalyst, 3 h), and (c) catalyst dosage (reaction condition: 3 h, T = 65 °C) on the conversion and selectivity for the liquid oxidation of BzOH to BzH.

This journal is © The Royal Society of Chemistry 2019

React. Chem. Eng., 2019, 4, 507–515 | 511

significantly decreased with increasing reaction temperature, indicating that a higher temperature is beneficial to the reaction process. In particular, the reaction could hardly progress, yielding BzOH conversion as low as 1.18% at a temperature of 40 °C. However, when the temperature rises to 80 °C, the conversion can reach 22.19%. The improvement in the catalytic efficiency is mainly due to the faster activation rate of H_2O_2 and stronger intermolecular collision at a higher reaction temperature. However, it is easy to deeply oxidize the obtained BzH to form the byproduct BzA at a higher temperature, which will result in lower selectivity. Fig. 4c shows the relationship between the catalytic performance and SG dosage. Apparently, the BzOH conversion was sharply improved from 7.06% (when the catalyst dosage is 1 mg) to 18.16% at 4 mg SG usage with an unchanged selectivity, indicating that the amount of catalyst plays an important role in the catalytic oxidation of BzOH. When the amount of SG was further increased to 5 mg, the conversion continues to increase, but the selectivity decreases significantly, which may be due to the further oxidation of BzH into BzA with an excess amount of catalyst. In addition to the intrinsic kinetics, the factors of agitation for this reaction system were also examined. As shown in Table S2,† when the stirring speed is 500 rpm, both the conversion and selectivity were slightly decreased when compared with the reaction that proceeded without stirring. However, as the rotational speed continues to increase, the conversion increases, but the selectivity remains at a relatively low level (about 91%). According to earlier studies, the catalytic oxidation of BzOH with the existence of H_2O_2 is a surface reaction, whose efficiency is considerably influenced by the chance of contact between the reactant and the catalyst. The reaction solution maintains a strong turbulent state when the stirring speed is high, which can considerably enhance the mass transfer efficiency between the reactants and the catalyst, thereby increasing the conversion of BzOH. Nevertheless, the strong turbulent state also increases the chance of contact between the reactant and the product with oxygen. Finally, the reaction proceeds with low selectivity due to the further oxidation of BzH. However, in general, the yield of the target product under stirring conditions is significantly higher than that without stirring.

In addition to investigating reaction kinetics, the reaction mechanism also needs to be investigated because a proper understanding of the chemical process can facilitate the design of more efficient catalysts. In the past several years, the reaction mechanism of BzOH oxidation catalyzed by metal catalysts has been thoroughly studied for its industrial importance in the manufacture of downstream chemicals.[47] With regard to carbon-based metal-free catalytic systems, some scholars have proposed that the difference between metal-free carbon-based materials and traditional metal catalysts is that nanocarbon can be directly used as a catalyst, rather than the generally recognized acid–base catalytic centers or metal-based active sites.[26] However, there is still a lack of the perfect mechanism and sufficient proof mechanism for metal-free catalysts, particularly sulfur-doped carbon ma-

terials. DFT calculations were carried out to gain a further fundamental understanding regarding the catalytic roles of SG sites and reaction mechanism. According to the EDS mapping results, it is revealed that there are oxygen atoms in the samples. Further, it is true that the oxygen-containing groups influence the catalytic performance of the SG catalyst. However, there is a considerable difference in the reaction path between the oxygen and sulfur active sites. It is well known that there are several studies that investigate the reaction mechanism by oxygen active sites. This paper aims at exploring the oxidation mechanism by sulfur-doped metal-free catalysts. Further, we have simplified the process. That is, only the introduction of sulfur atoms and its influence on the chemical and physical properties of carbon materials were considered. Generally, carbon atoms in ideal graphene molecules are highly symmetric and the energy distribution can be considered as 0 eV, which reveals weak catalytic activity. When the sulfur atom dopes into the graphene sheet, the energy distribution of the carbon atoms that are near the doped sulfur atom gets changed, which are most possibly considered as catalytic active sites (as depicted in Fig. 5a). Correspondingly, the final energy distribution of the four optimized sites is shown in Fig. 5b. These results show that the carbon adjacent to the sulfur atom possesses the lowest energy distribution of −0.08 eV, which indicates that this location is the most likely to be the active site of the reaction. Fig. 5c shows the density of states of SG and pristine graphite. The decrease in intensity of the induced localized electronic states on the carbon sites indicates the redistribution of electrons upon the formation of the doping of sulfur atom. Moreover, the energy changes at each step of the
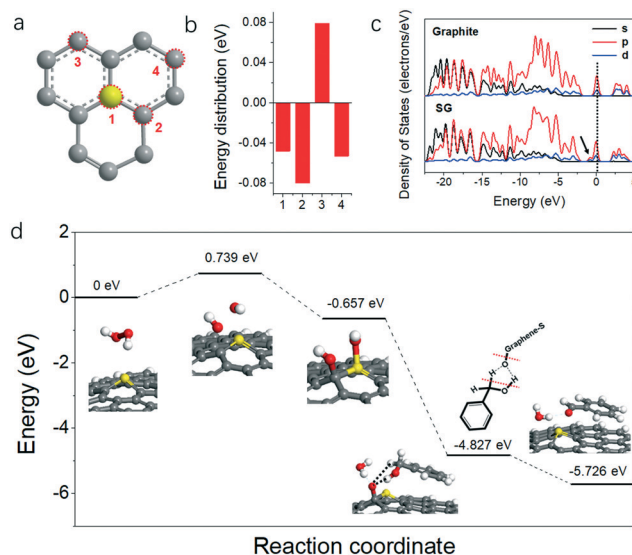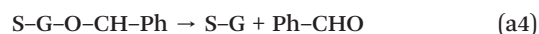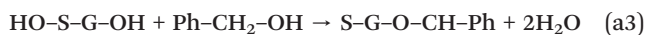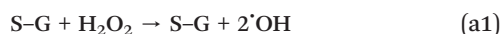

Fig. 5 (a) Models with different sites used in the DFT calculations; (b) corresponding adsorption energies at different sites; (c) density of states of s, p, and d orbitals of pristine graphite and SG; (d) reaction energy profile at different coordinates of the catalytic oxidation of BzOH by SG on active site 2 (gray, white, red, and yellow balls represent C, H, O, and S atoms, respectively).

512 | React. Chem. Eng., 2019, 4, 507–515

This journal is © The Royal Society of Chemistry 2019

reaction processes can be calculated in order to understand the process in a more precise manner. First of all, although H_2O_2 acts as an oxidant in the reaction, it is difficult to directly participate in the reaction as a molecule. Most studies have assumed that the H_2O_2 molecule can be decomposed into the hydroxyl radical (˙OH) under reaction conditions and then proceed with the subsequent steps. Fig. S6† shows the decomposition of one H_2O_2 molecule into two ˙OHs and adsorbed onto the surface of SG by two different paths, that is, two of the ˙OHs get adsorbed on the same site (such as sulfur atom and carbon atoms) or on different sites (one on the sulfur atom and the other on the carbon atom). According to the final adsorption state, we can observe that the absorbed ˙OHs are unstable and can easily react further to form water molecules when two ˙OHs get absorbed on one active site. In contrast, if the ˙OHs are adsorbed on different sites, it is easy to form two stable reactive oxygen species on the catalyst with a lower activation barrier (E_{T-2} = 0.739 eV < E_{T-1} = 0.926 eV), which indicates that the reaction is more likely to proceed by following the second path. Then, the reaction energy profile in Fig. 5d shows the formation of stable reactive oxygen species acting with the absorbed BzOH in a strongly exothermic process (energy: 4.17 eV) and the desorption of the target product, BzH, is 0.899 eV, which are moderate for a mild reaction condition. Therefore, based on the above evidence, the catalytic cycle process of the aerobic oxidation of BzOH over SG can be concluded in the following four steps. The H_2O_2 molecule was decomposed into two ˙OHs because of the SG catalyst under suitable reaction conditions (a1). Then, the dissociative ˙OH in the reaction solution was absorbed by SG at certain active sites to form HO–S–G–OH reactive oxygen species (a2). Next, BzOH molecules are adsorbed, which will induce further reactions of the two neighboring ˙OHs to generate water molecules; meanwhile, activated BzOH reacts with the reactive oxygen species on the surface of the SG catalyst (a3). Finally, BzH is obtained by desorption from the system, which provides active sites for the next cycle (a4).

$$S–G + H_2O_2 \rightarrow S–G + 2˙OH \quad\quad\quad (a1)$$

$$S–G + 2˙OH \rightarrow HO–S–G–OH \quad\quad\quad (a2)$$

$$HO–S–G–OH + Ph–CH_2–OH \rightarrow S–G–O–CH–Ph + 2H_2O \quad (a3)$$

$$S–G–O–CH–Ph \rightarrow S–G + Ph–CHO \quad\quad\quad (a4)$$

To verify the above hypothesis, a hydroxyl radical detection experiment was conducted by using methylene blue (MB) as a tracer agent. Generally, MB can react with the ˙OHs in the mixture at a certain ratio. Therefore, the relative concentration of ˙OHs can be obtained from MB consumption, which was measured using the 756PC UV-vis spectrometer at a wavelength of 664 nm according to Beer–Lambert's law.[48] Fig. S6† shows the MB consumption at different reaction conditions. Sample #1 was the reference sample that was fabricated without any additional reactions after maintaining for 3 h. When adding 1 mg catalyst (sample #2) or 1 mL H_2O_2 at room temperature, MB was decreased to about 6% and 12%, which can be attributed to the trace existence of ˙OH in water and H_2O_2 self-decomposition, respectively. The results of sample #2 and sample #4 indicates that a higher temperature can facilitate the generation of ˙OH. When comparing samples #4–#7, it is evident that the influence of the reaction temperature becomes more significant; further, stirring at 1000 rpm can promote the generation of ˙OH in the reaction mixture, which considerably facilitates the optimization of the experimental conditions.

Investigating the reaction mechanism is helpful in improving the efficiency of a catalytic reaction. However, in addition to this, the reaction degree is also influenced by the micro-mixing performance in process magnification including mass transfer efficiency. RPB, a typical apparatus that mimics a high-gravity environment, can significantly intensify micro-mixing and mass transfer in the liquid–liquid phase reaction system. Herein, we have carried out the experiment of BzOH oxidation in the RPB reactor to investigate the mechanism of PI in metal-free catalytic reactions. Fig. 6a shows a typical reaction process. First, a certain amount of aqueous BzOH and aqueous H_2O_2 (dispersed with 2 mg of SG catalyst, ultrasonic treatment for half an hour) were pumped into the RPB with a speed ratio of 60 : 1. The two liquid streams were pre-mixed at the inlet of the RPB and then sprayed by the slotted pipe distributor onto the inside edge of the packing. The mixture flowed through the packing in the radial direction under centrifugal force, and the resultant mixture flows out of the equipment through the liquid exit for collection. In order to ensure that the ratio between the reactant and catalyst is unchanged and more reliable, the resultant mixture in the collection tank was pumped into the RPB in the recycling mode when the reactants in both the tanks were exhausted, and the reactor was kept running at a rotating speed of 1500 rpm. Moreover, the circulating water was set at 60 °C. Fig. 6b shows the relationship between the catalytic performance and high-gravity level. Apparently, BzOH conversion was continuously improved from 5.56% at conventional gravity (1g) to 20.86% at a high-gravity level of 279g with unchanged selectivity. Similar variations were obtained by changing the amounts of treatment when the reactions were conducted in the RPB and beaker reactor (Fig. 6c). This indicates that a high-gravity level can considerably shorten the reaction time for BzOH oxidation. Generally, the surface renewal rate and turbulent kinetic energy in the reaction system are two main factors that influence surface catalytic reactions.[49] Fig. 6d shows the turbulent kinetic energy distribution of the reactant mixture in the RPB reactor simulated by CFD at different gravity levels. When the gravity level is 1g or lower, the turbulent kinetic energy is small and the distribution is uneven, which is unfavorable for catalytic reactions. However, with an increase in the gravity level, the magnitude of the turbulent kinetic energy

This journal is © The Royal Society of Chemistry 2019

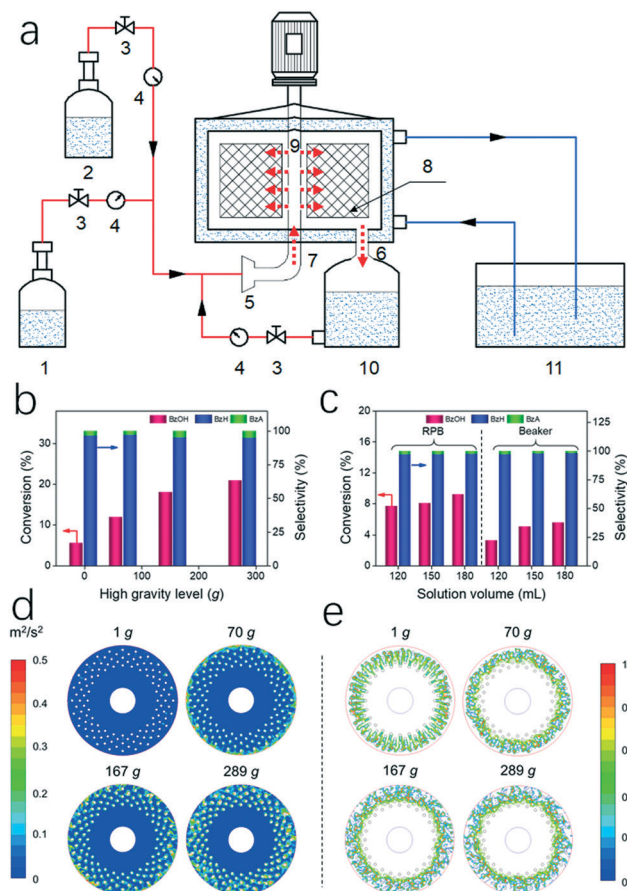React. Chem. Eng., 2019, 4, 507–515 | 513

Fig. 6 (a) Schematic diagram of the enhanced catalytic reaction process by high gravity (1: BzOH aqueous tank; 2: hydrogen peroxide aqueous tank; 3: feed flow controller; 4: flowmeter; 5: inlet; 6: outlet; 7: RPB; 8: wire mesh packing; 9: slotted pipe distributor; 10: product tank; 11: circulating water flume); effect of the (b) high-gravity level (reaction condition: 3 h, 2 mg catalyst, T = 60 °C), and (c) solution volume (reaction condition: 1 h, 2 mg catalyst, T = 60 °C) on the conversion and selectivity for the liquid oxidation of BzOH to BzH; (d) turbulent kinetic energy and (e) liquid proportion distribution of the reactant mixture simulated by CFD at different high-gravity levels (white dot represents the cross-section of the wire mesh packing).

increases, particularly around the wire mesh packing, which can be attributed to the collision between the mixture flow and rotating wire mesh. Meanwhile, when the liquid flow strikes the mesh, the mixture is either cut into a liquid line or a small droplet. As shown in Fig. 6e, the liquid proportion distribution of the reactant mixture in the RPB was calculated at different gravity levels; the blank area indicates gas, and the colored area indicates the existence of liquid and its amount. Therefore, the distribution morphology of the diagram basically represents the morphology of the actual liquid in the RPB reactor. Obviously, the higher the gravity level, the smaller is the cut of the liquid, which indicates a higher surface renewal rate and can provide additional chances of contact between the reactants and the catalyst, ultimately leading to higher catalytic efficiency.

Conclusions

In summary, an efficient SG metal-free catalyst for the liquid-phase catalytic oxidation of BzOH was fabricated by a well-developed ball-milling method. The reaction conditions were optimized as the BzOH conversion of 18.2% and BzH selectivity of 96.8% were obtained at different reaction temperatures, catalyst dosages, reaction times, and stirring speed. Followed by DFT calculations, we identified that the high catalytic activity is facilitated by the rearrangement of the electron cloud when sulfur atom is doped into the carbon skeleton, which can promote the decomposition of H_2O_2 molecules into hydroxyl radicals. Furthermore, a high-gravity RPB reactor was used and the BzOH conversion increased to 20.86%. Both experimental and CFD simulations indicated that the high-gravity level can provide more turbulent kinetic energy and faster surface renewal rate, resulting in more efficient collision chances between the reactants and the catalyst, ultimately leading to higher catalytic efficiency. This study not only expands the applications of SG in the catalytic oxidation process but also provides useful information about the potential practice of combining metal-free catalysts and high-gravity technology for the green synthesis of chemicals for a promising future.

Conflicts of interest

There are no conflicts to declare.

Acknowledgements

References

1 Z. Chai, T.-T. Zeng, Q. Li, L. Lu, W. Xiao and D. Xu, *J. Am. Chem. Soc.*, 2016, **138**, 10128–10131.

2 A. Gavriilidis, A. Constantinou, K. Hellgardt, K. K. Hii, G. J. Hutchings, G. L. Brett, S. Kuhn and S. P. Marsden, *React. Chem. Eng.*, 2016, **1**, 595–612.

3 Q. Yao and C.-J. Li, *Chem. Commun.*, 2017, **53**, 11225–11228.

4 J. B. Brazier, K. Hellgardt and K. K. Hii, *React. Chem. Eng.*, 2017, **2**, 60–67.

5 S. Peiris, J. McMurtrie and H.-Y. Zhu, *Catal. Sci. Technol.*, 2016, **6**, 320–338.

6 K. Hernandez, T. Parella, G. Petrillo, I. Uson, C. M. Wandtke, J. Joglar, J. Bujons and P. Clapes, *Angew. Chem., Int. Ed.*, 2017, **56**, 5304–5307.

7 D. D. Mal, S. Khilari and D. Pradhan, *Green Chem.*, 2018, **20**, 2279–2289.

8 H. Xia, Z. Liu, Y. Xu, J. Zuo and Z. Qin, *Catal. Commun.*, 2016, **86**, 72–76.

9 R. A. Sheldon and J. Dakka, *Catal. Today*, 1994, **19**, 215–245.

514 | *React. Chem. Eng.*, 2019, **4**, 507–515

This journal is © The Royal Society of Chemistry 2019

10 G. M. Mullen, E. J. Evans, B. C. Siegert, N. R. Miller, B. K. Rosselet, I. Sabzevari, A. Brush, Z. Duan and C. B. Mullins, *React. Chem. Eng.*, 2018, **3**, 75–85.

11 B. Jiang, H. Yang, L. Zhang, R. Zhang, Y. Sun and Y. Huang, *Chem. Eng. J.*, 2016, **283**, 89–96.

12 M. Li, Z. Zhou, F. Zhang, W. Chai, L. Zhang and Z. Ren, *AIChE J.*, 2016, **62**, 4023–4034.

13 J. Xie, P. Duan, N. Kaylor, K. Yin, B. Huang, K. Schmidt-Rohr and R. J. Davis, *ACS Catal.*, 2017, **7**, 6745–6756.

14 J. Xie, B. Huang, K. Yin, H. N. Pham, R. R. Unocic, A. K. Datye and R. J. Davis, *ACS Catal.*, 2016, **6**, 4206–4217.

15 J. Xie, K. Yin, A. Serov, K. Artyushkova, H. N. Pham, X. Sang, R. R. Unocic, P. Atanassov, A. K. Datye and R. J. Davis, *ChemSusChem*, 2017, **10**, 359–362.

16 X. Duan, H. Sun and S. Wang, *Acc. Chem. Res.*, 2018, **51**, 678–687.

17 B. Qiu, M. Xing and J. Zhang, *Chem. Soc. Rev.*, 2018, **47**, 2165–2216.

18 X. Liu and L. Dai, *Nat. Rev. Mater.*, 2016, **1**, 1–12.

19 S. T. Senthilkumar, S. O. Park, J. Kim, S. M. Hwang, S. K. Kwak and Y. Kim, *J. Mater. Chem. A*, 2017, **5**, 14174–14181.

20 J.-F. Chen, *Engineering*, 2017, **3**, 283–284.

21 D. Wang, Z. Wang, Q. Zhan, Y. Pu, J.-X. Wang, N. R. Foster and L. Dai, *Engineering*, 2017, **3**, 402–408.

22 V. P. Pham, H.-S. Jang, D. Whang and J.-Y. Choi, *Chem. Soc. Rev.*, 2017, **46**, 6276–6300.

23 V. Georgakilas, J. A. Perman, J. Tucek and R. Zboril, *Chem. Rev.*, 2015, **115**, 4744–4822.

24 Y. Zhang, X. Fan, J. Jian, D. Yu, Z. Zhang and L. Dai, *Energy Environ. Sci.*, 2017, **10**, 2312–2317.

25 Z. Wang, Y. Pu, D. Wang, J. Shi, J.-X. Wang and J.-F. Chen, *AIChE J.*, 2018, **64**, 1330–1338.

26 Z. Wang, R. Su, D. Wang, J. Shi, J.-X. Wang, Y. Pu and J.-F. Chen, *Ind. Eng. Chem. Res.*, 2017, **56**, 13610–13617.

27 X.-K. Kong, C.-L. Chen and Q.-W. Chen, *Chem. Soc. Rev.*, 2014, **43**, 2841–2857.

28 Y. Pu, J. Leng, D. Wang, J. Wang, N. R. Foster and J. Chen, *Chin. J. Chem. Eng.*, 2018, **26**, 2206–2218.

29 R. Ascrizzi, J. González-Rivera, C. S. Pomelli, C. Chiappe, P. Margari, F. Costagli, I. Longo, M. R. Tiné, G. Flamini and C. Duce, *React. Chem. Eng.*, 2017, **2**, 577–589.

30 U.S. Department of Energy, Chapter 6: Innovating Clean Energy Technologies in Advanced Manufacturing, in *Quadrennial Technology Review*, U.S. Department of Energy, Washington, DC, 2015.

31 U.S. Department of Energy, An assessment of energy technologies and research opportunities, in *Quadrennial Technology Review*, U.S. Department of Energy, Washington, DC, 2015.

32 R. J. M. Westerhof, S. R. G. Oudenhoven, P. S. Marathe, M. Engelen, M. Garcia-Perez, Z. Wang and S. R. A. Kersten, *React. Chem. Eng.*, 2016, **1**, 555–566.

33 Y. Pu, J. Leng, D. Wang, J. Wang, N. R. Foster and J. Chen, *Powder Technol.*, 2018, **340**, 208–216.

34 Y. Pu, F. Cai, D. Wang, J.-X. Wang and J.-F. Chen, *Ind. Eng. Chem. Res.*, 2018, **57**, 1790–1802.

35 G.-W. Chu, J. Fei, Y. Cai, Y. Liu, Y. Gao, Y. Luo and J.-F. Chen, *Ind. Eng. Chem. Res.*, 2018, **57**, 2329–2335.

36 Y. Luo, J.-Z. Luo, G.-W. Chu, Z.-Q. Zhao, M. Arowo and J.-F. Chen, *Chem. Eng. Sci.*, 2017, **170**, 347–354.

37 T. Lin, Y. Tang, Y. Wang, H. Bi, Z. Liu, F. Huang, X. Xie and M. Jiang, *Energy Environ. Sci.*, 2013, **6**, 1283–1290.

38 E. Zhang, G.-P. Hao, M. E. Casco, V. Bon, S. Grätz and L. Borchardt, *J. Mater. Chem. A*, 2018, **6**, 859–865.

39 P. Kolla, C. Lai, S. Mishra, H. Fong, W. Rhine and A. Smirnova, *Carbon*, 2014, **79**, 518–528.

40 A. Stolle, T. Szuppa, S. S. Leonhardt and B. Ondruschka, *Chem. Soc. Rev.*, 2011, **40**, 2317–2329.

41 Y. Wang, D. Wang, M. Tan, B. Jiang, J. Zheng, N. Tsubaki and M. Wu, *ACS Appl. Mater. Interfaces*, 2015, **7**, 26767–26775.

42 J. Xu, J. Shui, J. Wang, M. Wang, H. Liu, S. Dou, I.-Y. Jeon, J.-M. Seo, J.-B. Baek and L. Dai, *ACS Nano*, 2014, **8**, 10920–10930.

43 L. Zhao, X.-L. Sui, Q.-Y. Zhou, J.-Z. Li, J.-J. Zhang, G.-S. Huang and Z.-B. Wang, *J. Mater. Chem. A*, 2018, **6**, 6212–6219.

44 S. Mahamulkar, K. Yin, P. K. Agrawal, R. J. Davis, C. W. Jones, A. Malek and H. Shibata, *Ind. Eng. Chem. Res.*, 2016, **55**, 9760–9818.

45 C. Liu, R. Tan, D. Yin, N. Yu and Y. Zhou, *Chin. J. Catal.*, 2010, **31**, 1369–1373.

46 C. Kamonsatikul, T. Khamnaen, P. Phiriyawirut, S. Charoenchaidet and E. Somsook, *Catal. Commun.*, 2012, **26**, 1–5.

47 A. Savara, C. E. Chan-Thaw, J. E. Sutton, D. Wang, L. Prati and A. Villa, *ChemCatChem*, 2017, **9**, 253–257.

48 S. Zhang, D. Wang, P. P. Fan and L. P. Sun, *Desalin. Water Treat.*, 2015, **57**, 1–10.

49 M. Nemanashi and R. Meijboom, *J. Colloid Interface Sci.*, 2013, **389**, 260–267.

This journal is © The Royal Society of Chemistry 2019

React. Chem. Eng., 2019, **4**, 507–515 | 515